Modeling rip current circulations and vorticity in a high-energy mesotidal-macrotidal environment

N. Bruneau, Philippe Bonneton, Bruno Castelle, Rodrigo Pedreros

Modeling rip current circulations and vorticity in a high-energy mesotidal-macrotidal environment

N. Bruneau,[1,2] P. Bonneton,[2] B. Castelle,[2] and R. Pedreros[3]

Received 29 September 2010; revised 29 March 2011; accepted 7 April 2011; published 28 July 2011.

[1] In June 2007 an intense 5 day field experiment was carried out at the mesotidal-macrotidal wave-dominated Biscarrosse Beach on a well-developed bar and rip morphology. Previous analysis of the field data elucidated the main characteristics of a tide-modulated and strongly evolving rip current driven by low- to high-energy shore-normal waves. Here we present a modeling strategy based on the vertically integrated and time-averaged momentum equations accounting for roller contribution that is applied to the Biscarrosse experiment. Wave and flow predictions in the surf zone improve significantly when using a spatially constant time-varying breaking parameter by Smith and Kraus (1990). The model correctly reproduces the main evolving behaviors of the rip current. An advection-diffusion equation governing the mean wave-driven current vertical vorticity is further derived from the momentum equations. Vertical vorticity is driven by a forcing term that depends on the breaking wave energy dissipation and on the wave propagation direction. Spatial gradients in depth-induced broken-wave energy dissipation therefore determine both the strength and the sign of the wave-driven circulation rotational nature. When applied to the Biscarrosse experiment, the vorticity efficiently predicts the main characteristics of the evolving rip current such as its width, cross-shore extension, and intensity. In addition, good correlations are found between the maximum rip current intensity and the deviation of the forcing term. Thus, we determine precisely the rotational component associated with the wave forcing which is less direct through the traditional radiation stress approach.

Citation: Bruneau, N., P. Bonneton, B. Castelle, and R. Pedreros (2011), Modeling rip current circulations and vorticity in a high-energy mesotidal-macrotidal environment, *J. Geophys. Res.*, *116*, C07026, doi:10.1029/2010JC006693.

1. Introduction

[2] Rip channels are commonly observed along wave-dominated sandy barred beaches. They appear quasi-rhythmically as depressions in shore-connected or unconnected shoals [*Quartel*, 2009]. Counterrotating circulations characterized by seaward flowing jets in the rip channel are driven by waves on these bed forms when waves approach at an angle close to shore normal. These narrow, intense (reaching 1–2 m/s) currents are called rip currents. Understanding and predicting the complex dynamics of rip currents remain a relevant scientific challenge because they play a key role on the beach and surf zone morphodynamics, on the dispersion of material across the surf zone and are a major hazard to swimmers [*Brown et al.*, 2009; *MacMahan et al.*, 2006, 2010; *Thornton et al.*, 2007; *Reniers et al.*, 2009]. While topographically controlled rip currents have received increasing attention these last decades [*MacMahan et al.*, 2006], major advances in the understanding of rip current kinematics that recently challenged traditional views of rip current behaviors [*Reniers et al.*, 2010; *MacMahan et al.*, 2010; *Castelle et al.*, 2010] show that rips are still poorly understood and therefore motivate further rip studies.

[3] Documented rip studies have mostly been restricted to low-energy microtidal rip currents over small alongshore bed nonuniformities [*Brander*, 1999; *MacMahan et al.*, 2005, 2010; *Reniers et al.*, 2007]. Rip current investigations in high-energy environments are still poorly documented [*Brander and Short*, 2000; *Castelle et al.*, 2006; *Bruneau et al.*, 2009a], particularly over strongly alongshore nonuniform beaches. Intense mean rip currents, reaching 1 m/s, were measured near the rip neck by *Brander and Short* [2000] for moderate-energy wave conditions. More recently, *Bruneau et al.* [2009a] measured high-energy topographically controlled mean rip currents (around 0.9 m/s) for low-energy waves ($H_s \approx 0.9$ m). In addition, they highlighted the evolving behavior of rip currents in an energetic mesotidal-macrotidal environment with (1) a strong tidal modulation during low-energy wave conditions ($H_s < 1$ m) and (2) the presence of intense undertow during energetic events ($H_s > 2.5$ m) that dominates the surf zone dynamics.

[1]Laboratório Nacional de Engenharia Civil, Lisbon, Portugal.
[2]Environnements et Paléoenvironnements Océaniques et Continentaux, UMR 5805, Université Bordeaux 1, CNRS, Talence, France.
[3]BRGM, Orléans, France.

0148-0227/11/2010JC006693

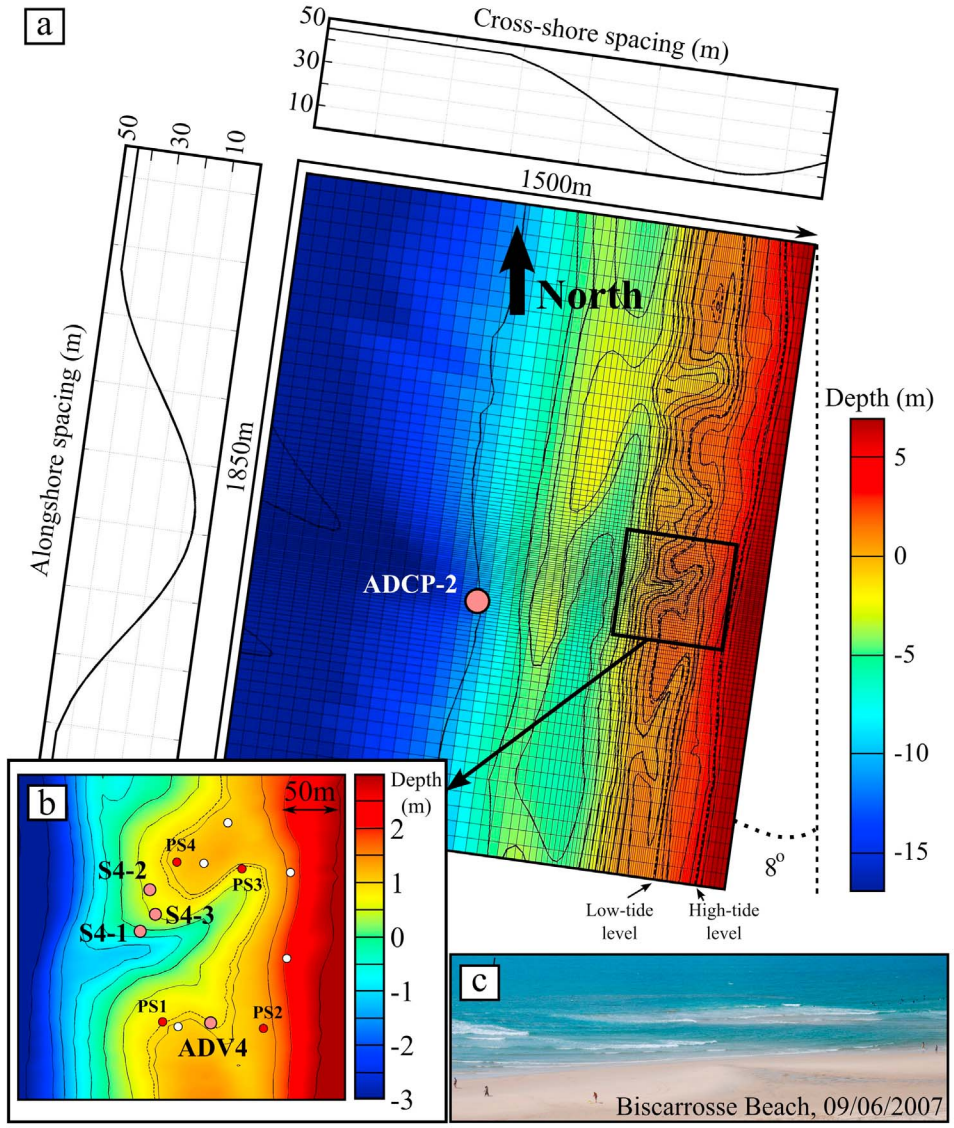

Figure 1. Biscarrosse Beach bathymetry. (a) Irregular rectangular full grid superimposed on the bathymetry with (top) the cross-shore grid spacing and (left) the alongshore grid spacing. (b) Zoom on the instrumented bar and rip morphology showing the locations of the sensors; large light circles for the main sensors involved in the study, small dark circles for other sensors used herein, and small white circles for unused sensors. (c) Photograph of the bar and rip morphology prior to the start of the field experiment.

[4] Combination of field and numerical investigations is currently one of the most promising avenues for rip current analysis because numerical modeling can provide important information when measurements are difficult to obtain. Many modeling studies based on laboratory or field works have focused on the hydrodynamics of rip currents through a depth-averaged or quasi-three-dimensional approach [*Haas et al.*, 2003; *Castelle et al.*, 2006; *Castelle and Bonneton*, 2006; *Bruneau et al.*, 2008, 2009b]. These studies have shown the ability of these models to reproduce the wave-driven horizontal circulations and low-frequency rip current motions generated by shear instabilities [*Haller and Dalrymple*, 2001; *Özkan-Haller and Kirby*, 1999] or forced by wave grouping [*Reniers et al.*, 2007]. Recently, *Reniers et al.* [2009, 2010] used a full three-dimensional model to compute surface flow fields to investigate material dispersion and surf zone retention. However, most of these works were restricted to microtidal environments with low-energy waves over small alongshore seabed nonuniformities.

[5] As shown theoretically by *Peregrine* [1998], nonuniformities along the breaking-wave crest drive vertical vorticity. He modeled the breaking event as the development of a surface and current discontinuity in the nonlinear shallow water equations and proceeded to a direct analysis of the vorticity at the wave time scale. These processes induce mean vorticity with horizontal scales larger than the local water depth; rip currents are a good example of these macrovortices. Retention, dispersion and generally vortical motions associated with topographically controlled rip currents are linked to both quasi-stable rip current, bipolar

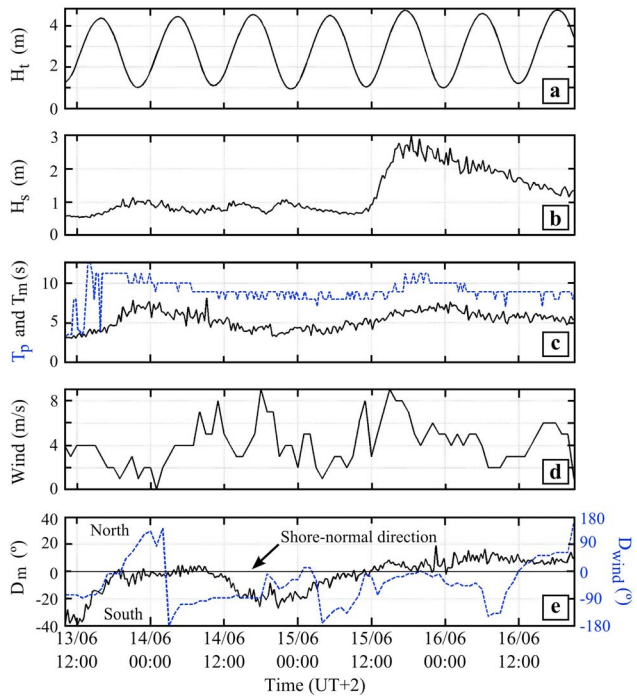

Figure 2. Offshore wave and tide forcings during the 4 days simulated in the study. (a) Tide level H_t, (b) significant wave height H_s, (c) peak T_p (dashed line) and mean T_m (solid line) periods, (d) wind speed and (e) mean wave direction D_m (solid line) and wind direction (dashed line).

circulation cells and unstable, nonstationary jets. *Bühler* [2000] and *Bühler and Jacobson* [2001] described a general theoretical analysis of wave-driven currents and vortex dynamics due to dissipating waves. In addition, they demonstrated that mean flow vorticity generation is controlled by dissipative forces. Based on the system of equations presented by *Smith* [2006], *Bonneton et al.* [2010] identified a vorticity forcing term related to differential, broken-wave energy dissipation as the main source of vorticity.

[6] To examine topographically controlled wave-driven circulations and to investigate evolving rip current behaviors in this study, we use a numerical model based on the nonlinear shallow water equations presented by *Ardhuin* [2005] and *Smith* [2006]. Our model is applied to the Biscarrosse 2007 field experiment [*Bruneau et al.*, 2009a] to validate wave and flow simulations. Next, the mean vorticity conservation equation [*Bruneau et al.*, 2008; *Bonneton et al.*, 2010] is applied to a complex mesotidal-macrotidal high-energy rip current system. The predictive capability of the vertical vorticity conservation equation is further used to investigate the evolving behavior of a rip current for a wide range of tide levels and wave conditions.

2. Study Area

2.1. Regional Setting

[7] The Aquitanian coast is a mesotidal-macrotidal high-energy environment exhibiting a strongly alongshore non-uniform and variable double sandbar system. The outer and the inner bars usually exhibit crescentic patterns, and bar and rip morphologies, respectively [*Castelle et al.*, 2007; *Almar et al.*, 2010]. As with all of the wave-dominated Aquitanian Coast beaches, the Biscarrosse Beach is exposed to high-energy North Atlantic swells coming mainly from the W-NW direction, with an annual mean significant wave height H_s of about 1.4 m and a mean period T_m near 6.5 s [*Butel et al.*, 2002]. During a severe storm, the offshore wave height can reach 10 m. The annual mean spring tidal range is approximately 3.7 m, and the maximum tidal range reaches 5 m.

2.2. Field Experiment: Biscarrosse 2007

[8] An extensive description of the experiment is given by *Bruneau et al.* [2009a]. Figure 1 shows the nearshore bathymetry surveyed during the experiment with concurrent forcing conditions given in Figure 2. During the field experiment, the tidal range varied from 3.3 to 3.8 m (Figure 2a). Offshore significant wave height (H_s) ranged from 0.5 to 3 m (Figure 2b) with persistent swell and only scarcely a superimposed wind sea. Peak wave period (T_p) ranged from 8 to 11 s (Figure 2c) with a wave approach persistently close to the shore normal (Figure 2e). Wind magnitude and direction are given in Figures 2d and 2e, respectively.

[9] The instrumented well-developed bar and rip morphology was characterized by a narrow and deep rip channel (Figures 1b and 1c). As detailed by *Bruneau et al.* [2009a], an array of in situ stationary instruments (Figure 1b) was deployed on this intertidal inner bar and rip system between 13 and 17 June. In the present study, we focus on the S4 and ADV4 records (Figure 1b) because they are the longest samples and were deployed in relevant locations: the rip neck and the southern feeder, respectively. The nearshore morphology did not change significantly during the course of the experiment as only a weak onshore migration of the bar was captured through video imagery [*Bruneau et al.*, 2009a].

3. Modeling Strategy

[10] The modeling strategy consists in coupling the spectral wave model SWAN [*Booij et al.*, 1999] with the nonlinear shallow water model MARS [*Lazure and Dumas*, 2008]. The sediment transport module [*Bruneau et al.*, 2007; *Bruneau*, 2009] is not activated in the present study.

3.1. Wave Model

[11] Wave transformation is computed with the spectral wave model SWAN [*Booij et al.*, 1999] that solves the wave action density balance equation. In our approach, SWAN is used in stationary mode to simulate the wave propagation and deformation. In addition, the effects of generation, dissipation (breaking, bottom friction), nonlinear wave-wave interactions (triad) are taken into account. The wave-current interactions are switched off. An irregular rectangular grid (Figure 1a) is used with a coarse resolution (45 m) along both the offshore and the lateral boundaries. The area of interest is meshed with a 6 m resolution. The computational grid resolution is detailed in Figure 1a. Finally, 36 directions (10° resolution) and 20 frequencies (corresponding to periods varying logarithmically from 2 to 20 s) are used for the directional and spectral discretizations, respectively.

[12] Two parameters are set in the present work: (1) the breaking wave parameter γ_b (wave height-to-depth ratio) and (2) the friction coefficient. The breaking parameter is crucial because it controls the rate of wave energy decay within the surf zone. In the present study, two breaking wave parameters were investigated: (1) a constant γ_b of 0.73 (default value of SWAN) and (2) a spatially constant but time-varying γ_b computed according to the formulation of *Smith and Kraus* [1990]:

$$\gamma_b = \frac{1.12}{1+e^{-60m}} - 5.0\left[1+e^{-43m}\right]s_\infty \tag{1}$$

where m is the mean shoreface slope (herein we use a constant value of 0.02 which allows good wave predictions, as demonstrated later) and s_∞ is the deep-water wave steepness (ratio between the offshore wave height and the offshore wavelength). In addition, γ_b has a minimum threshold of 0.5 to prevent underestimation of the significant wave heights during the energetic period when the model of *Smith and Kraus* [1990] predicts low values of γ_b (which can reach 0.3). This boundary is in agreement (same order) with the work of *Bertin et al.* [2009] which bounded the γ_b with values ranging from 0.4 to 0.8. This formulation is used for its simplicity of implementation (no full-iterative method required; the new breaking parameter is only computed from the previous wave simulation results) and for the good results obtained by *Bertin et al.* [2009]. The equivalent roughness length, K_n, proposed by *Madsen et al.* [1988] is set to 0.04 m to overall fit with the data.

[13] Offshore wave and tide forcing was provided by the ADCP-2 (Figure 1a) deployed in 10 m water depth (at low tide) seaward of the study area and offshore of the subtidal bar. Wave spectra are specified at each boundary (both offshore and lateral) to avoid potential wave energy shadow areas. Finally, both the wave conditions and the water level are updated every 20 min to compute the new wavefield, which is short enough in a mesotidal-macrotidal environment.

3.2. Shallow Water Flow Model

[14] MARS is a finite difference model, originally designed to compute tide- and wind-induced currents. It has been extensively tested on the whole French coast (*http://www.previmer.org/en*). MARS solves the nonlinear shallow water equations in two or three dimensions (it is used in the depth-averaged mode herein).

[15] Most of the depth-averaged models that compute wave-induced currents are based on the radiation stress approach [*Longuet-Higgins and Stewart*, 1964]. *Dingemans et al.* [1987, p. 539] and *Battjes* [1988] showed that the "formulation of the driving forces in terms of the wave dissipation yields more trustworthy results than those obtained by numerical differentiation of the radiation stress tensor." In addition, *Svendsen* [1984] showed the dominance of the roller in dissipating wave energy in the surf zone. During the field experiment, the surf similarity parameter ranged from 0.1 to 0.3 characterizing the dominance of spilling waves which justifies the choice to use a roller model. Thus, according to the works of *Ardhuin* [2005] and *Smith* [2006], and defining $\vec{U}$ as the mean depth-averaged velocity vector and $\overline{\zeta}$ as the mean free surface elevation, the hydrodynamic system of equations can be written as follows (the different stages to obtain these equations with the roller contribution are detailed in Appendix A):

$$\partial_t\overline{\zeta} + \partial_i\overline{h}U_i = -\partial_i\tilde{Q}_i \tag{2}$$

$$\partial_t U_i + U_j\partial_j U_i + g\partial_i\overline{\zeta} = -\partial_t\tilde{J} + \frac{D^r k_i}{\sigma_r\rho\overline{h}} + \frac{\tilde{Q}_j}{\overline{h}}\left(\partial_i U_j - \partial_j U_i\right) + \frac{H_i}{\rho\overline{h}} + \frac{\overline{\tau}_i^S - \overline{\tau}_i^B}{\rho\overline{h}} \tag{3}$$

where t is time, g is the gravitational acceleration, ρ is the fluid density, $\overline{h}$ is the mean water depth, H_i is the lateral turbulent shear stress and, τ_i^S and τ_i^B are the surface and bottom shear stresses, respectively. Finally, defining k_i as the wave number and σ_r as the relative frequency, the terms related to the waves (superscript w for the wave-organized motion and superscript r for the roller) can be described as mass transport of unbroken and broken waves Q_i^w and Q_i^r, respectively:

$$\tilde{Q}_i = Q_i^w + Q_i^r = \left(E^w + E^r\right)\frac{k_i}{\rho c k} \tag{4}$$

and the irrotational contribution to radiation stresses J^w and J^r:

$$\tilde{J} = J^w + J^r = \frac{E^w}{\rho\overline{h}}\left(\frac{c^g}{c} - \frac{1}{2}\right) + \frac{E^r}{2\rho\overline{h}} \tag{5}$$

with E^w and E^r the organized wave motion and roller energy, respectively, c and c^g are the phase and group celerities, respectively, ρ_r is the mass density of the roller and A_r is the area of the roller computed with the following balance equation: $\partial_t E^r + \partial_i[E^r\,(U_i + c_i)] = D^w - D^r$, where D^w is the wave energy dissipation computed according to *Battjes and Janssen* [1978]. The wave energy is classically defined as $E^w = \rho_g {H_{rms}}^2/8$, and the roller energy is evaluated with the formulation proposed by *Stive and De Vriend* [1994] and *Dally* [2001], that is, $E^r = \rho_r c A_r/T_m$. The roller energy dissipation is given by $D^r = g\beta_D E^r/c$ [*Dally and Brown*, 1995; *Dally*, 2001] with β_D a constant set to 1.

[16] The surface and bottom friction are given by

$$\overline{\tau}_i^S = \rho\ 0.0015\ \|\vec{U}^{Wind}\|\ U_i^{Wind} \tag{6}$$

$$\overline{\tau}_i^B = \frac{2}{\pi}\rho\ C_f\ \|\vec{U}^w\|\ U_i \tag{7}$$

where U^{Wind} is the wind velocity at 10 m and U^w is the wave orbital velocity magnitude. The friction coefficient C_f is set to 0.006.

[17] Defining $\nu_{t,i}$ as the horizontal turbulent eddy viscosity coefficient, the mixing term H_i is parameterized as

$$H_i = \rho\overline{h}\partial_j\left(\nu_{t,i}\partial_j U_i\right) \tag{8}$$

According to *Battjes* [1975], the wave breaking is the main process governing the mixing in the surf zone. In addition,

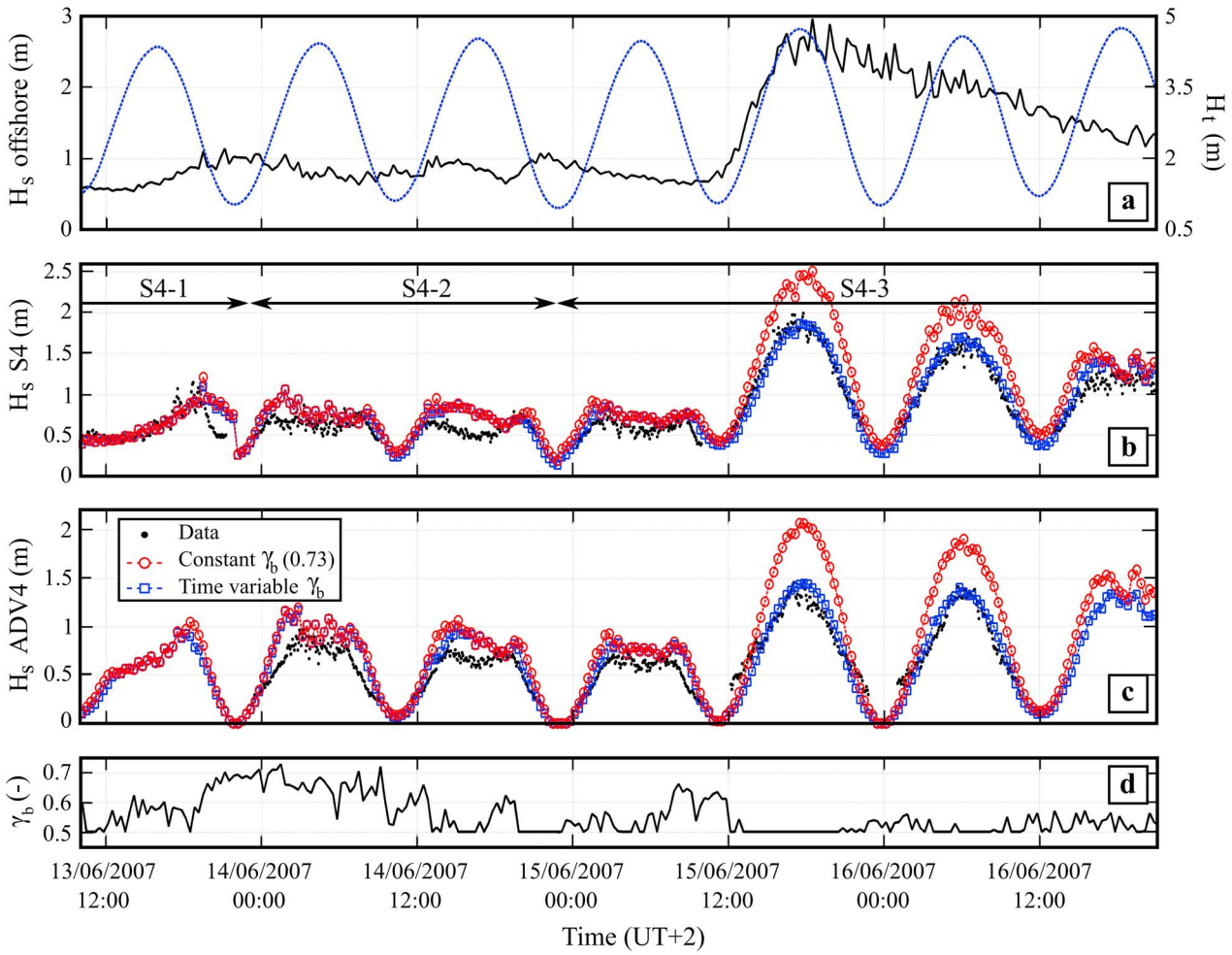

Figure 3. Time series of (a) offshore wave height (solid line) and tidal elevation (dashed line) and the comparisons between measured and modeled significant wave height at (b) the three S4 locations and (c) ADV4 for a constant breaking parameter (dashed line with circles) and for a time-varying breaking parameter (dashed line with squares). (d) The evolution of the computed time-varying breaking parameter γ_b.

considering small scale eddies associated to submesh processes, the global turbulent eddy viscosity $\nu_{t,i}$ coefficient is computed as follows:

$$\nu_{t,i} = M\bar{h}\left(\frac{D^w}{\rho}\right)^{1/3} + f_v\ 0.01\ \Delta_{s,i}^{1.15} \tag{9}$$

where M is a constant set to 7, f_v is 3 $m^{0.85}/s$ and $\Delta_{s,i}$ is the spacing in the i direction.

[18] To account for tide level variations, the signal recorded by the ADCP-2 (denoted H_t in Figure 2a) is imposed at the offshore boundary. Periodic lateral conditions are used. Thus, only a cross-shore propagation of the tide is modeled in this approach. Finally, a constant hydrodynamic time step of 0.8 s is used to solve the nonlinear shallow water equations on the same irregular rectangular grid as for SWAN (Figure 1a). To compute the mean currents and to filter the far-infragravity and infragravity current motions, a 20 min averaging is applied to the computed currents.

4. Application to the Biscarrosse Beach

4.1. Wave Simulations

4.1.1. Significant Wave Heights

[19] Figure 3 shows the comparison of the simulated significant wave height with that measured at the two sensors for both constant and time-varying breaking parameter. Results show that wave heights are significantly overestimated during the energetic event ($H_s > 2$ m) when using the constant default breaking parameter ($\gamma_b = 0.73$). The overestimation reaches 0.7 m for offshore significant wave heights of 2.5–3 m (25%). Using a time-varying γ_b improves the model ability to reproduce wave heights in the surf zone. The values of γ_b are illustrated in Figure 3d. During the low-energy period (the four first tidal cycles), γ_b ranges from 0.5 to 0.75 with a mean value of around 0.6–0.65 while

Table 1. RMS Errors Between the Significant Wave Height Measured and the Modeled

Sensors	S4	ADV4	PS1	PS2	PS3	PS4
Constant γ_b	29 cm	33 cm	27 cm	22 cm	15 cm	20 cm
Variable γ_b	14 cm	16 cm	16 cm	14 cm	11 cm	17 cm

it remains close to 0.5–0.55 during the energetic event. Table 1 summarizes the root-mean-square (RMS) errors obtained with the two γ_b parameterizations for a larger set of sensors. The use of the spatially constant but time-varying γ_b improves the results considerably (RMS errors of about 15 cm) with a halving of the RMS errors (about 30 cm with the constant γ_b). In addition, the correlation coefficients obtained between the data and the model predictions are greater than 0.9.

[20] For the time-varying γ_b, the results (Figure 3) show that (1) for both low-energy and high-energy conditions the model underestimates the wave heights at low-tide levels and (2) for low-energy waves the model overestimates wave heights around the midtide levels. The third cycle shows a contrasting behavior with a strong overprediction at high tide that is correlated with a significant wind event.

4.1.2. Ratio Between Wave Height and Depth: γ

[21] Figure 4 shows the time series of $\gamma = H_s/\overline{h}$ at two representative locations. Similar to previous comparisons of wave heights, the model is in good agreement with field data. During low-energy periods, both constant and time-varying γ_b curves fit well with the data while during the energetic event, the use of a time-varying γ_b substantially improves the model accuracy. Particularly, the ADV4 recordings (Figure 4b) highlight a threshold with a value $\gamma = 0.35$. This threshold is well represented with the variable γ_b but is strongly overestimated when using a constant γ_b that induces a saturation of γ at a value of 0.5. This behavior clearly shows that wave-energy dissipation through depth-induced breaking over a complex bar and rip morphology cannot be accurately modeled if using a time-invariant breaking parameter γ_b.

[22] Overall, the wavefields predicted by SWAN using a spatially constant and time-varying breaking parameter are in good agreement with the data obtained during the field experiment for both low-energy and high-energy periods. The RMS errors are on the order of 15 cm, which is reasonably low to subsequently investigate the topographically controlled wave-driven circulations.

4.2. Hydrodynamic Simulations

4.2.1. Offshore Mean Currents

[23] Wave and flow data were acquired outside the surf zone throughout the experiment by ADCP-2 deployed offshore of the crescentic subtidal outer bar (Figure 1a). The comparison between these (depth-averaged) mean flow data and the model results is given in Figure 5. For the cross-shore mean velocities (Figure 5a), the order of magnitude is well reproduced with currents lower than 5 cm/s and a clear tidal signal. For energetic conditions, weak offshore currents (undertow of about 15 cm/s) due to wave breaking over the outer bar are modeled, while no undertow is present in the measured sample. Figure 5b illustrates the major impact of wind on the alongshore currents. The data-model agreement improves significantly when wind is taken into account. Hence, only the simulations accounting for wind stresses are presented below. Of note, the tide signal is weakly visible (Figures 5b and 5c).

[24] To investigate the hydrodynamics above the outer bar during the full campaign, Figure 6 details the temporal evolution of the modeled cross-shore currents along an alongshore profile, located offshore of the outer bar (Figure 6a). During low-energy conditions, when waves do not break across the outer bar, flows are characterized by weak tide-induced

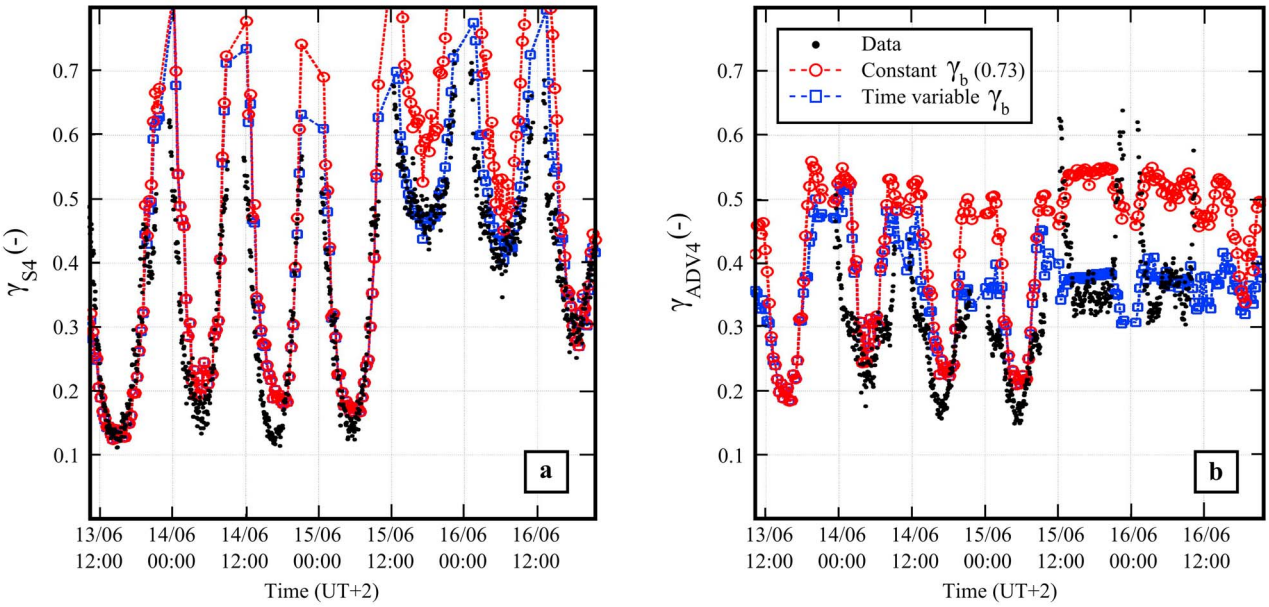

Figure 4. Time series of γ at (a) S4 and (b) ADV4. Black dots represent the measurements; the dashed line with squares (circles) illustrates the model results for a time-varying (constant) breaking parameter.

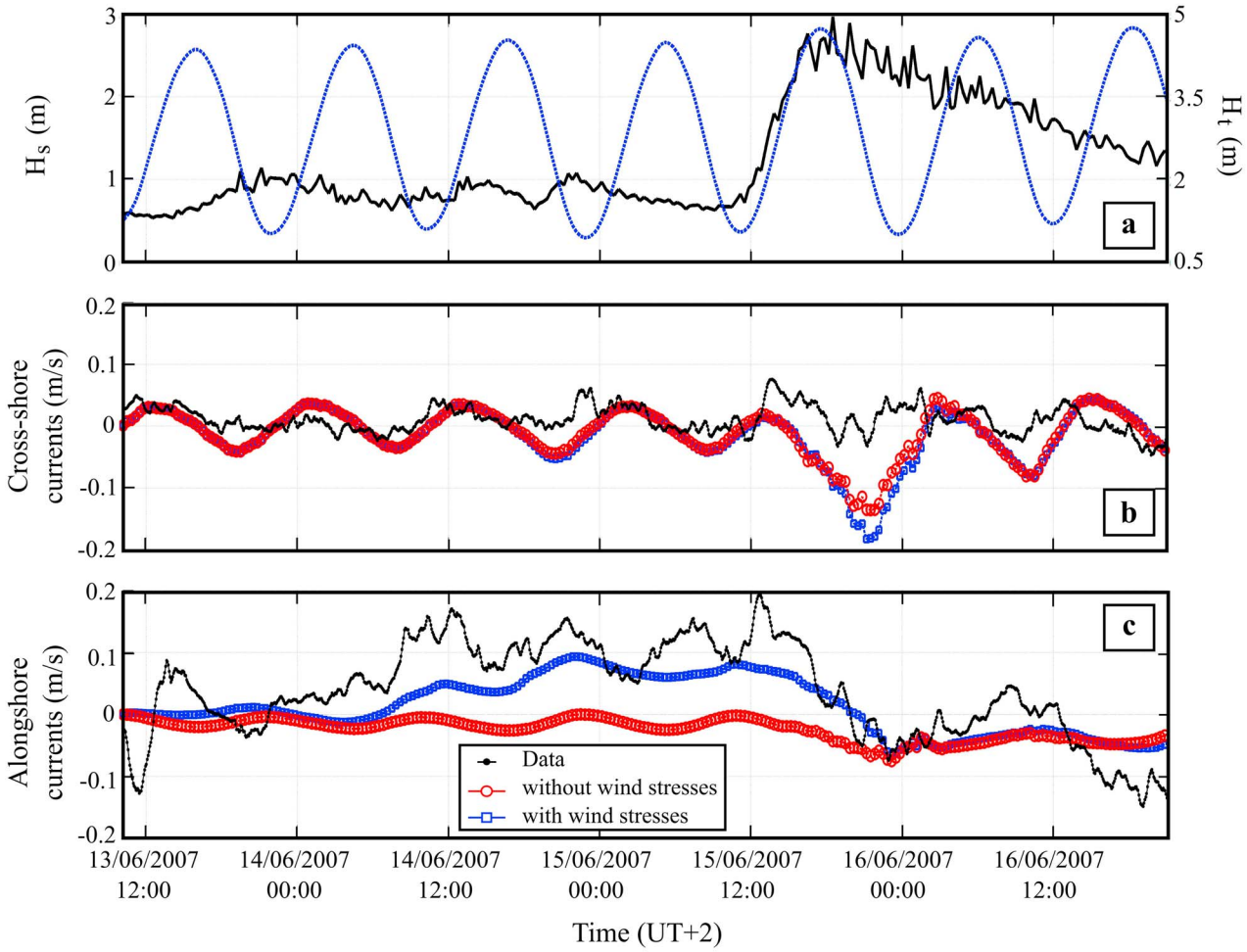

Figure 5. Time series of offshore 20-min-averaged currents (depth-averaged) at the ADCP-2 location. Time series of (a) offshore wave height (solid line) and tidal elevation (dashed line) and (b) cross-shore 20-min-averaged and depth-integrated velocity measured (black dots) and modeled without wind surface stresses (circles) and with wind surface stresses (squares). (c) Time series of 20-min-averaged and depth-integrated alongshore velocity. By convention, positive (negative) cross-shore currents indicate onshore- (offshore-) directed currents and positive (negative) alongshore currents indicate northward (southward) directed currents.

currents. With increasing offshore wave heights, waves break across the outer bar inducing a large offshore wave-driven circulation with onshore-directed currents across the crescent horn and offshore currents across the crescent bay. Figure 6c shows the strong alongshore variability of the cross-shore currents during the energetic conditions. Particularly, offshore (onshore) currents are weaker (stronger) at 50 m northward of the ADCP-2 (inducing better comparisons with the data in Figure 5).

4.2.2. Rip Current Behavior on a Mesotidal-Macrotidal Beach

[25] Figure 7 shows both the cross-shore and the alongshore components of the 20-min-averaged currents for the three locations of the S4 current meter (on the edge of the rip neck) and the ADV4 (southern feeder). For both the cross-shore and the alongshore directions and also for both the S4 and the ADV4, the flow behaviors are qualitatively reproduced by the model.

[26] Rip and feeder currents during the low-energy period are characterized by (1) strong mean currents (>0.4 m/s) between low and midtide with a maximum value reached between low and midtide and (2) weak currents between midtide and high tide (<0.05 m/s). This intense tide modulation is well predicted by our approach (RMS error less than 0.1 m/s and correlation coefficients in the order of 0.6–0.85 except for the alongshore currents at the S4 location where the correlation coefficient is of 0.25). When the S4 was deployed close to the rip neck (S4-1), both data and model results show the presence of a strong rip current (reaching 0.75 m/s) despite reasonably low-energy wave conditions (H_s < 1 m). At S4-2 and S4-3 locations (on the edge of the bar), the results (data and model in Figure 7b) indicate onshore-directed currents for low tide levels. With increasing tide levels from low to midtide, the breaking line shifts onshore and both measurements and model results show offshore-directed currents (rip currents). For the alongshore

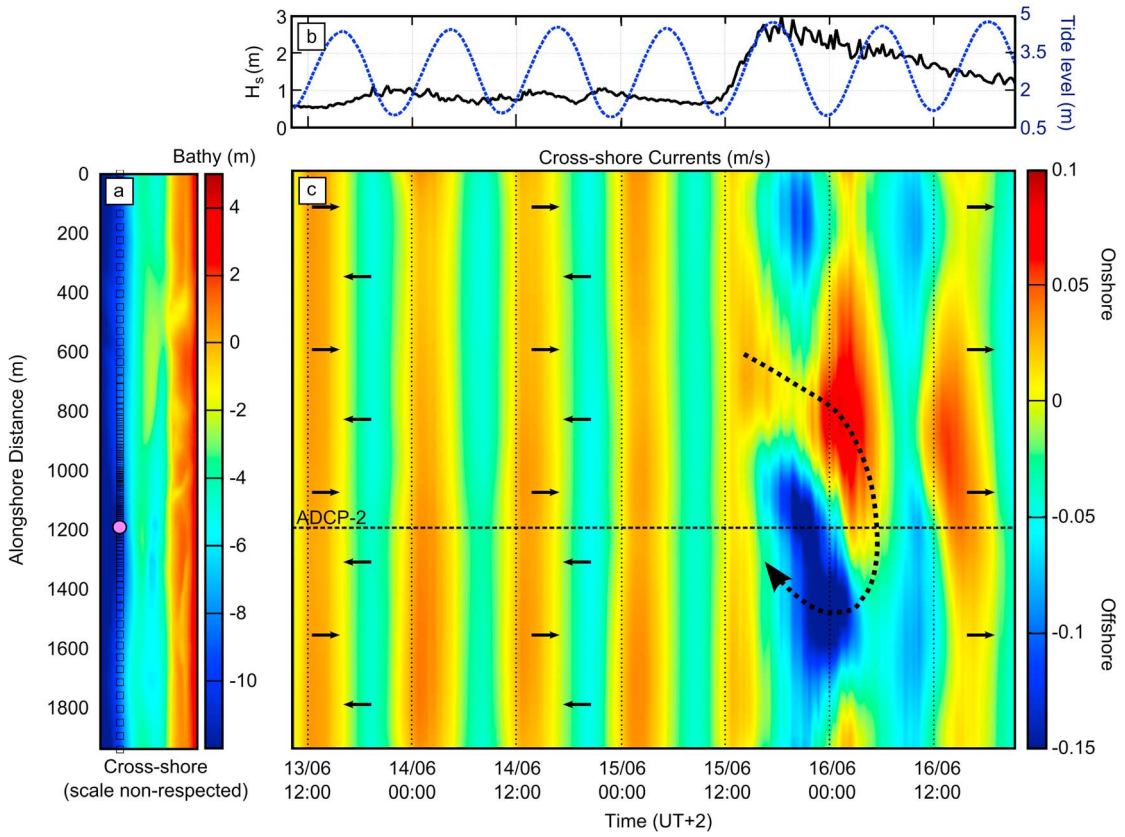

Figure 6. (a) Bathymetry with an unscaled cross-shore direction. Each square represents a node where cross-shore velocities are exported. (b) Time series of offshore significant wave height (solid line) and tidal levels (dashed line). (c) Time series of cross-shore currents along the alongshore profile. Dark and dotted arrows represent current directions.

currents (Figures 7c and 7e), overall, the model predictions are good despite a systematic small underestimation of the velocity (Figure 7e).

[27] When energetic conditions occur (from 15 June, 12:00 LT), strong offshore-directed currents are measured by both the S4 and the ADV4. The model underestimates this behavior with only weak offshore-directed currents (RMS errors <0.20 m/s and correlation coefficients of 0.4–0.7). During the first energetic cycle, the model computes onshore currents when the data show the presence of offshore currents (Figure 7d). On the one hand, these results point out the potential difficulties to model strong undertow with a depth-averaged approach where the vertical variability of the currents is not taken into account (see existing 3D modeling investigations of rip currents by *Haas et al.* [2003], *Reniers et al.* [2009], and *Haas and Warner* [2009]). On the other hand, the alongshore currents (Figures 7c and 7e) are well reproduced by the model. Finally, results obtained 3–4 grid meshes northward of the ADV4 location show better agreement with the data (Figure 10f; flow field during the energetic event with the presence of offshore directed currents northward of the ADV4), which suggests the potential impact of the bathymetry on obtaining good flow predictions. It illustrates the efficiency of the model to reproduce qualitatively the complex dynamics of rip currents even during an energetic event.

[28] Both the model and the data highlight the asymmetric behavior of the currents between the rising and the falling tide (Figures 7b and 7d). During the low-energy period, for similar offshore wave conditions, results at the S4 location show more intense rip current during the decreasing tide. In contrast, the ADV4 (onshore currents) shows lower onshore currents during the decreasing tide than during the rising tide.

5. Analysis of Rip Current Circulation Generation

5.1. Source Terms of the Momentum Equations

[29] As explained in section 3, the wave forcing in the momentum equations is composed by three driving source terms in equation (3): (1) $-\partial_i J$, (2) $D^r k_i/\sigma_r \rho \overline{h}$ and (3) $(\widetilde{Q}_j/\overline{h})(\partial_i U_j - \partial_j U_i)$. Figure 8 displays the spatial distributions of the intensity and directions of each term for offshore shore-normal waves with H_s = 1 m and T_p = 9 s. The first source force (irrotational), mainly linked to H_s^2, is directed seaward offshore of the breaking point due to the shoaling and onshore in the surf zone (Figure 8a). Further inshore, this term is directed from the edge of the bar to the rip neck due

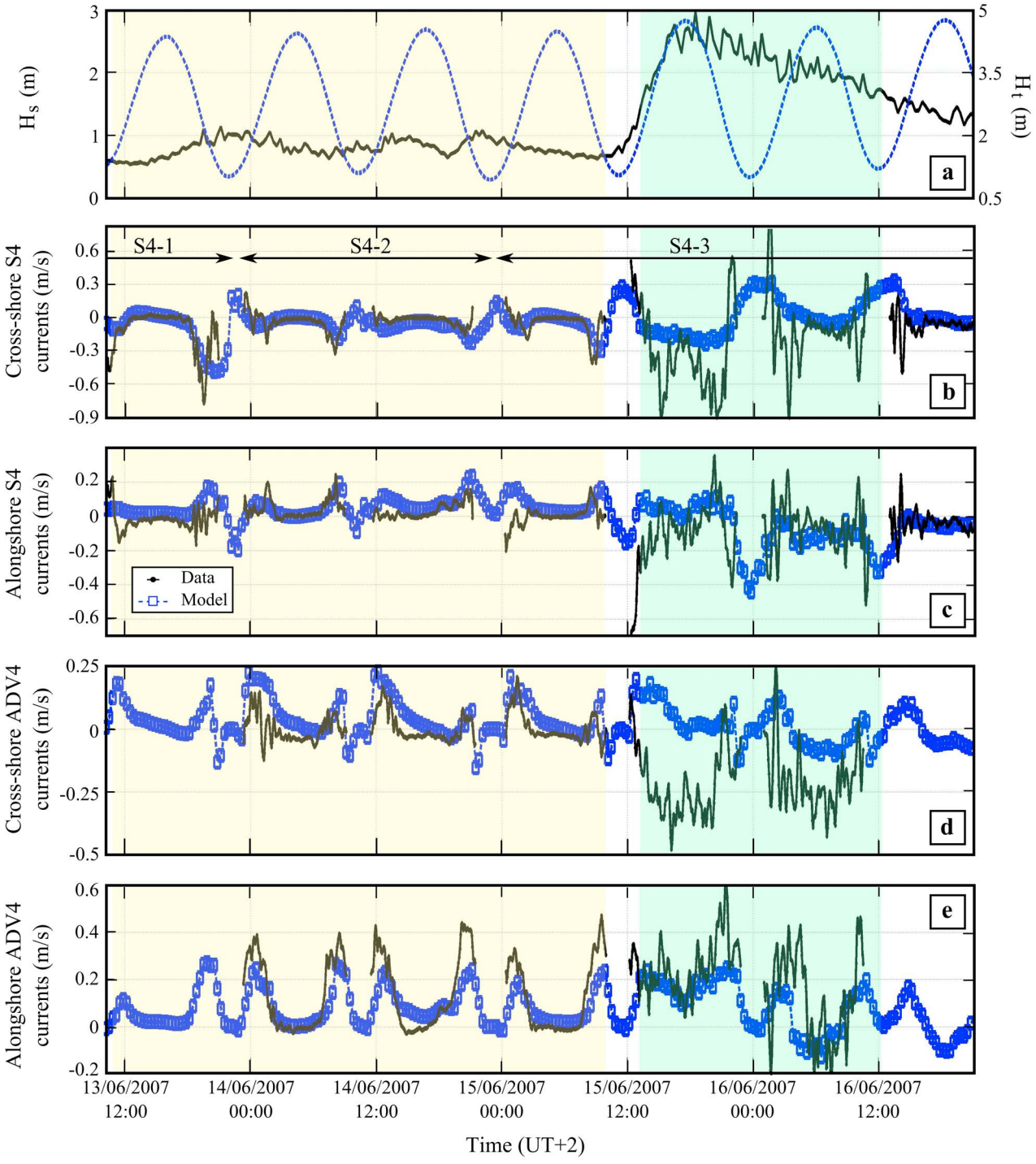

Figure 7. Time series of (a) offshore wave height (solid line) and tidal elevation (dashed line), (b) 20-min-averaged cross-shore current at S4-1, S4-2 and S4-3, (c) 20-min-averaged alongshore current at S4-1, S4-2 and S4-3, (d) 20-min-averaged cross-shore at ADV4, (e) 20-min-averaged alongshore at ADV4. In Figures 7b–7e the data are represented by black dots and model results are represented by the dashed line with squares. By convention, positive (negative) cross-shore currents indicate onshore- (offshore-) directed currents and positive (negative) alongshore currents indicate northward (southward) directed currents. The two shaded areas define two different rip behaviors: tidal modulation for low-energy waves and undertow during energetic conditions.

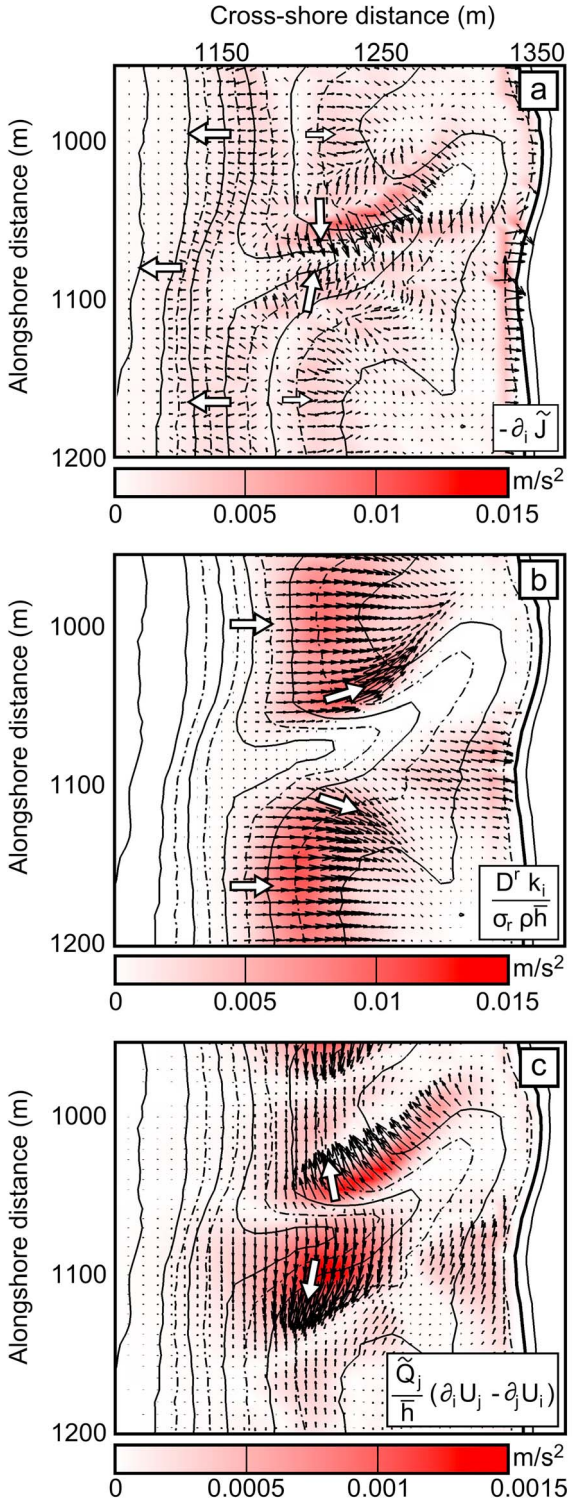

Figure 8. Comparison of the modeled wave source terms of the momentum equations for a midtide condition and a typical wave climate (H_t = 1.75 m, H_s = 1 m, T_p = 9 s with a shore-normal incidence): (a) $-\partial_i \tilde{J}$, (b) $D^r k_i/\sigma_r \rho \bar{h}$ and (c) $(\tilde{Q}_j/\bar{h})(\partial_i U_j - \partial_j U_i)$. The arrows represent the main direction of the forcing.

to wave refraction. The second term, which is driven by the energy dissipation, is significant above the bar where waves break and almost vanishes in the rip channel (Figure 8b). In addition, this term follows the wave propagation rays. Finally, the last term (called vortex force) is only persistent at the rip edges and is directed from the channel to the edges. While this source is smaller than the two previous ones, it tends to compensate the first term and to strengthen the jet as it was suggested by *Ardhuin* [2005]. The formulation used herein provides a decomposition of the driving source forces to interpret wave-induced currents and circulations.

5.2. Vorticity Theory

[30] Previous studies [*Bühler*, 2000; *Bühler and Jacobson*, 2001] presented a general theoretical analysis of wave-driven currents and vortex dynamics due to dissipating waves. In the present approach, as it is defined in equations (2) and (3), irrotational and rotational terms are clearly dissociated (which is not the case when considering the radiation stress approach). According to the previous works of *Bruneau et al.* [2008] and *Bonneton et al.* [2010] and

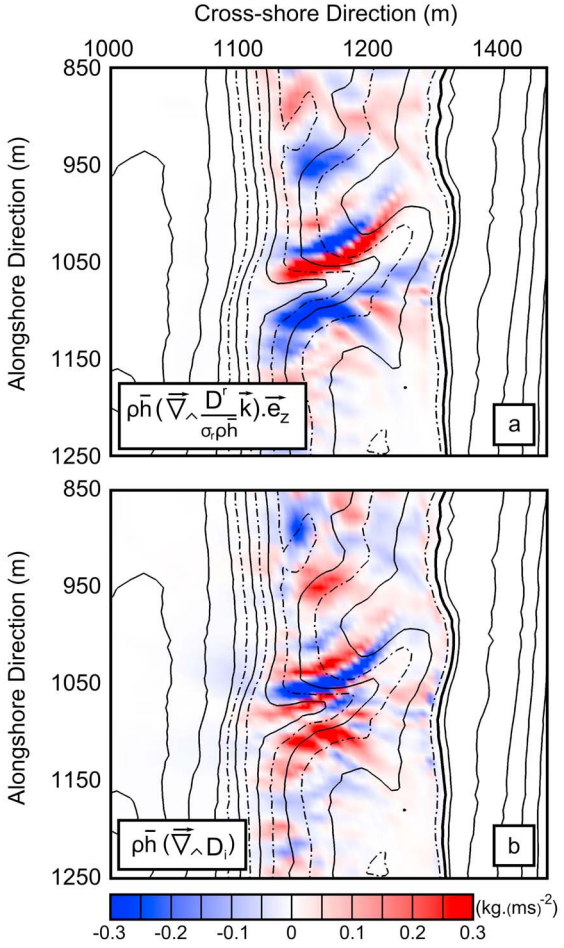

Figure 9. Snapshots of the two main source terms (model) of the vorticity conservation equation for a low-tide/midtide condition and a typical wave climate (H_t = 1.75 m, H_s = 1 m, T_p = 9 s with a shore-normal incidence): (a) the vorticity forcing term and (b) the diffusion term.

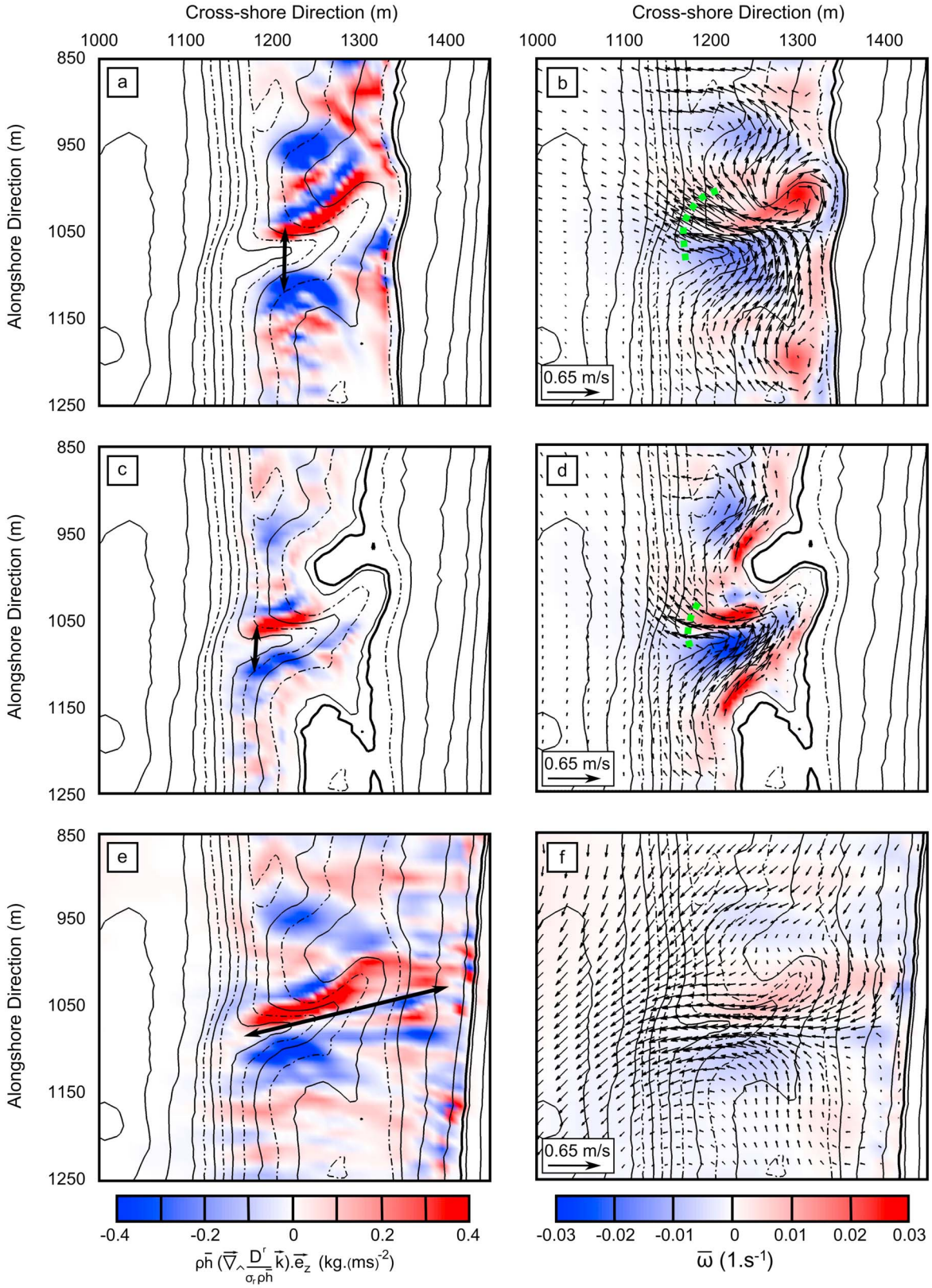

Figure 10. Snapshots of the vorticity forcing term calculated from the modeled wavefield (Figures 10a, 10c, and 10e) and the computed 20-min-averaged vorticity and currents at three contrasting moments (Figures 10b, 10d, and 10f) on (a and b) 14 June at 08:30 LT (UT + 2), (c and d) 14 June at 10:30 LT (UT + 2) and (d and e) 15 June, at 17:50 LT (UT + 2). Black arrows indicate cell separation distance or cell cross-shore extension and dotted green curves, Figures 10b–10d, give the rip width.

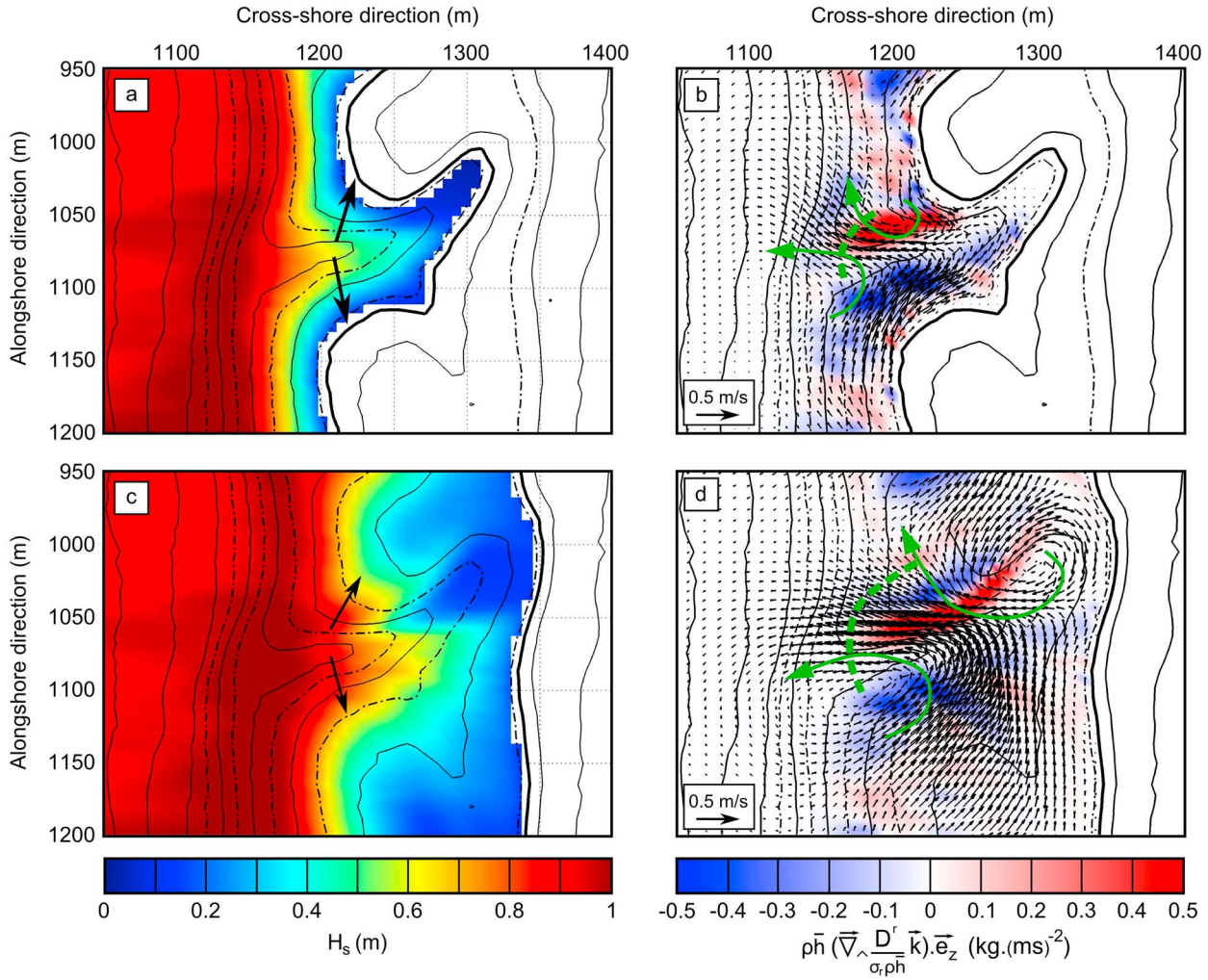

Figure 11. Example of rip current enlargement with increasing tide levels for a typical wave climate, H_s = 1 m, T_p = 9 s with a shore-normal incidence. Snapshots of the significant wave heights (Figures 11a and 11c) and the modeled vorticity forcing term superimposed on the modeled velocity field at two different instants (Figures 11b and 11d) for (a and b) low-tide H_t = 0.75 m and (c and d) low-tide/midtide H_t = 1.75 m. Black arrows indicate the significant wave height gradients, and the large dash-dotted line indicates the position where waves start to break. Dashed green curves show the rip width.

neglecting the friction term (that is around one order of magnitude lower than the two others in the surf zone), we can derive the mean vorticity $\overline{w} = (\vec{\nabla}\wedge\vec{U})\cdot\vec{e}_z$ conservation equation (only along the vertical in a two-dimensional approach) that reads:

$$\partial_t\overline{w} + \vec{\nabla}\cdot\left[\overline{w}\left(\vec{U}+\frac{\vec{\bar{Q}}}{\bar{h}}\right)\right] = \left(\vec{\nabla}\wedge\left[\frac{D^r}{\sigma_r\rho\bar{h}}\vec{k}\right]\right)\cdot\vec{e}_z + \left(\vec{\nabla}\wedge H_i\right).\vec{e}_z \tag{10}$$

According to the linear theory, the first term of the right-hand side can be simplified to $(\vec{\nabla}(D^r/\sigma_r\rho\bar{h})\wedge\vec{k})\cdot\vec{e}_z$. For a constant eddy viscosity coefficient ν_t, the second source term of equation (10) can be rearranged into a turbulent diffusion term $\nu_t\nabla^2\overline{w}$. The two terms of the right-hand side describe the production and the dissipation of mean vorticity, respectively. The production term is only active in presence of breaking waves, when the gradient of dissipation is not collinear with the wave propagation direction. Figure 9 presents both the eddy turbulent diffusion term and the term linked to the wave dissipation, which are of the same order of magnitude. The two terms in the left-hand side of equation (10), the local variation of the vorticity and advection, are small when the other two terms are active (not shown). Hence, the two main terms compensate more or less one another and the forcing term associated with the wave dissipation controls the mean flow vorticity. As the wave dissipation forcing term is the source of the vorticity, this modeled forcing and vorticity terms have good correlations (>0.7 and close to 1 near the rip edges).

[31] This formulation is a simple and efficient tool to investigate the generation of circulation cells in the surf zone, such as rip currents. This approach proved its efficiency to understand vortical motions of a rip current above an idealized bar and rip morphology [*Bonneton et al.*, 2010].

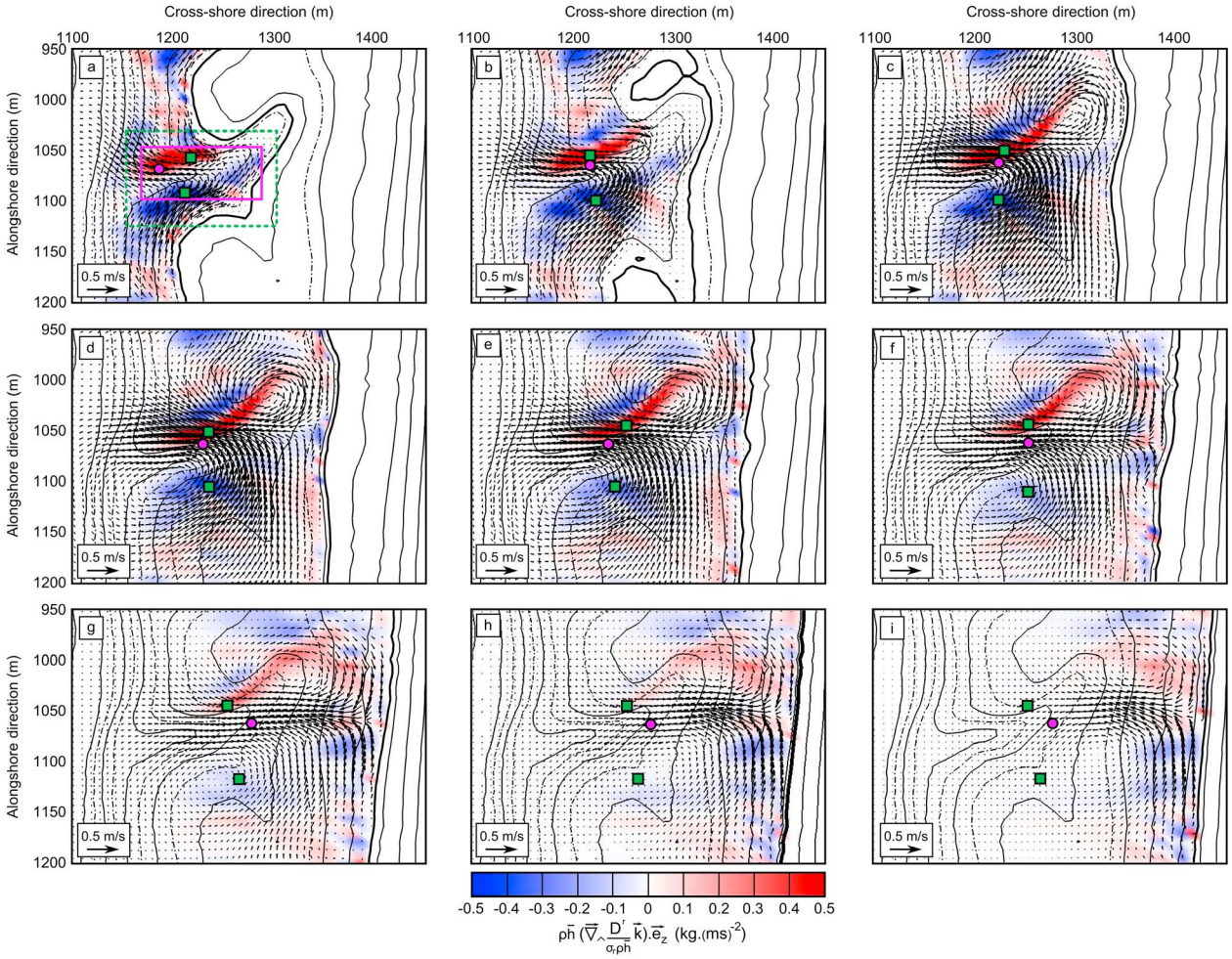

Figure 12. Snapshots of the computed vorticity forcing term superimposed on the modeled currents for different tide levels of (a) H_t = 0.75 m, (b) H_t = 1.25 m, (c) H_t = 1.75 m, (d) H_t = 2.25 m, (e) H_t = 2.75 m, (f) H_t = 3.25 m, (g) H_t = 3.75 m, (h) H_t = 4.25 m and (i) H_t = 4.75 m. Wave conditions are the same as in Figure 11. Squares give the position of the relative maxima and minima of the forcing term, and circles indicate the location of the maximum rip currents. The two boxes in Figure 12a illustrate the domain where local extrema are identified: dashed green box for the vorticity forcing term and purple box for the maximum rip velocity.

In the present work, we focus on a complex field bar and rip morphology (Biscarrosse field experiment presented above), both to investigate the validity of equation (10) and to improve our knowledge on the generation of wave-driven circulation in a high-energy rip current system.

5.3. Application to Biscarrosse Beach

[32] The theory detailed in section 5.2 is now applied to the Biscarrosse experiment to analyze the behavior of the forcing term $(\vec{\nabla} \wedge [\frac{D^r}{\sigma_r \rho \bar{h}} \vec{k}]) \cdot \vec{e}_z$ and its impact on the mean wave-driven circulations for different wave and tide conditions. Figure 10 describes three different forcing conditions: (1) at midtide, for low-energy waves, 14 June at 08:30 LT (UT + 2) (Figures 10a and 10b), (2) at low tide, for low-energy waves, 14 June at 10:30 LT (Figures 10c and 10d) and (3) close to high tide with energetic waves, 15 June at 17:50 LT (Figures 10e and 10f). In Figure 10c, the distance between the two vorticity cells is very small inducing a narrow and intense rip current (around 30 m wide, Figure 10d). With increasing tide levels (Figure 10a), the distance separating the two main cells increases, widening the rip throat (around 90 m wide, Figure 10b). Finally, Figures 10e and 10f show a cross-shore extension of the forcing term cells due to both the high-tide level and a larger surf zone (energetic waves). These extended and narrow shapes tend to illustrate the weak character of the rotational nature of mean currents with a low alongshore variability which characterizes the presence of undertow.

5.4. Main Predicted Behaviors of the Rip Current

[33] To investigate in depth the physical processes driving rip current circulations, we consider a typical low-energy condition (H_s = 1 m, T_p = 9 s and a shore-normal incidence). As the rip current is not active at high tide for this low-energy wave forcing [*Bruneau et al.*, 2009a], only two tide levels are investigated here: a low-tide level (H_t = 0.75 m)

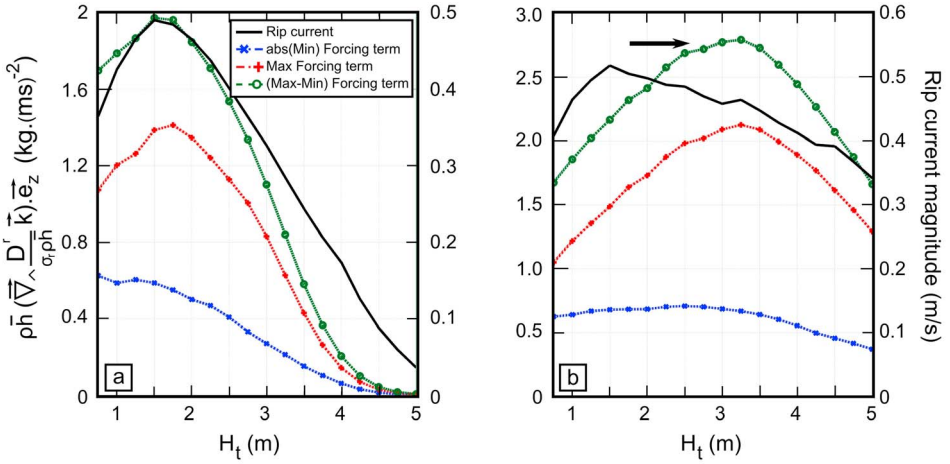

Figure 13. Evolution of both the modeled rip current magnitude (solid line) and the characteristics of the modeled forcing term (minimum (crosses), maximum (pluses) and the gradient maximum-minimum (circles)) function of the tide levels (model results) (a) for low-energy waves (H_s = 1 m, T_p = 9 s with a shore-normal incidence) and (b) for energetic conditions (H_s = 2 m, T_p = 9 s with a shore-normal incidence).

and a low tide/midtide level (H_t = 1.75 m). Figure 11 details both the wavefield (H_s) and the mean vorticity forcing term with superimposed mean currents. At low tide, when sandbars are not submerged, waves mostly break offshore of the bar and rip morphology. Wave refraction close to the bar is weaker (Figure 11a), but an important alongshore gradient of H_s is present between the rip channel and the edges of the bars (Figure 11a) that induces two circulation cells. The centers of these circulations are close and they are located in the edge of the rip current system. The flows are drained from the shoals to the deepest part of the rip channel through a narrow jet (Figure 11b, 40 m wide and rip currents of 0.41 cm/s).

[34] For higher tide levels (mid tide), when sandbars are submerged, wave refraction is stronger over the bar and rip morphology (Figure 11c) but alongshore gradients of H_s are weak. Both the distance between the two cells and the intensity of the forcing term increase. Hence, the rip current widens and its velocity increases (Figure 11d, 80 m wide rip currents of around 0.48 cm/s).

[35] Figure 12 details the spatial evolution of the mean vorticity forcing term during a full tide cycle for low-energy conditions. Except at low tide, the maximum rip current intensity is located between the two extrema of the forcing term (but not systematically in the middle). Even though the rip current maximum is always located close to the most significant extremum, no clear correlation was found between maximum rip current locations and the forcing term intensity. With increasing tide levels, the forcing term cells extend in the cross-shore direction. The maximum rip current magnitude increases from low tide to low-tide/midtide levels (compare Figure 13a, black curve) and subsequently decreases rapidly when waves break onshore of the bar and rip morphology. In the meantime, the intensity of the forcing term also decreases. Both maximum rip current magnitudes and characteristics of the vorticity forcing term are illustrated in Figure 13 as a function of the tide level for low-energy shore-normal waves (Figure 13a, H_s = 1 m) and more energetic waves (Figure 13b, H_s = 2 m). Figure 13 shows the strong correlation between the rip current magnitude and the gradient between the maximum and the minimum of the forcing term (correlation greater than 0.95, except for the energetic wave conditions; Table 2). For low-energy conditions, the occurrence of maximum rip current between low tide and midtide is well predicted by the min/max gradient of the forcing term. For a more energetic event, the peak of the gradient is obtained for a higher tide level than the maximum rip current magnitude. The correlation coefficients for the min/max gradient are very good (correlation > 0.95) except for the shore-normal energetic conditions (0.45). In addition, the quality of the correlation coefficients (between the modeled forcing term and the modeled vorticity field) is not affected by wave direction or period at the offshore boundary (Table 2).

[36] These examples illustrate the potential of the formulation proposed above. From a computed wavefield on a given morphology, it is possible to investigate the shapes of the circulations and some characteristics of the rip current such as its location, its width and its extension. The good correlations obtained between the maximum rip current and the min/max deviation demonstrate the capacity of the approach to characterize the intensity of rip currents. The proposed model provides an useful and simple tool to investigate the vortical motions. Thus, computing the vertical vorticity conservation equation from a wavefield

Table 2. Correlation Coefficient (CC) Between the Rip Current Magnitudes and the Gradient Max-Min of the Forcing Term

H_s (m)	T_p (s)	Wave Type	CC
1	9	shore-normal	0.98
1	6	shore-normal	0.97
1	12	shore-normal	0.97
2	9	shore-normal	0.45
1	9	15° incidence N	0.95
1	9	15° incidence S	0.99

efficiently determines the strength and sign of the wave-driven circulation rotational nature, which is not possible with the traditional radiation stress approach.

6. Conclusions

[37] In this paper, a modeling strategy based on the depth-averaged and time-averaged momentum equations accounting for roller contribution was presented and applied to an evolving rip current system at the mesotidal-macrotidal Biscarrosse Beach. Computed wave heights and wave-driven currents show good agreement with field data using the spatially constant and time-varying breaking parameter suggested by *Smith and Kraus* [1990].

[38] In addition, we derived a conservation equation of the vertical vorticity of the mean wave-driven currents. This equation shows that the vorticity forcing term $(\vec{\nabla} \wedge [(D^r/\sigma_r \rho \overline{h})\,\vec{k}]) \cdot \vec{e}_z$, due to spatial gradients in broken-wave energy dissipation, is the only major source of topographically controlled wave-driven circulations. This term allows a straightforward qualitative prediction of some rip current characteristics such as its width, location, cross-shore extension or intensity. Good correlations are found between maximum rip current intensity and the gradient between the maximum and the minimum of the forcing term. Therefore, spatial gradients in depth-induced broken-wave energy dissipation determine both the strength and the sign of the rip current system rotational nature. Thus, computing this simple vertical vorticity conservation equation from a wavefield provides straightforward information on rip current circulations that was difficult to interpret through the traditional radiation stress approach.

Appendix A: Nonlinear Shallow Water Equations

[39] This appendix details the derivation of equations (2) and (3) given in section 3.2. The following is from the work by *Smith* [2006], where the roller distribution was included. Neglecting the Coriolis forces, the basic system of equations to solve the hydrodynamics in the surf zone, according to *Phillips* [1977] and accounting for the roller contribution [*Dally*, 2001], is given by

$$\partial_t \overline{\zeta} + \partial_i \overline{h} U_i = -\partial_i \tilde{Q}_i \tag{A1}$$

$$\partial_t U_i + U_j \partial_j U_i + g \partial_i \overline{\zeta} = -\frac{1}{\rho \overline{h}} \partial_j (S_{ij} + R_{ij}) - \frac{1}{\overline{h}} \partial_j \left[U_j \tilde{Q}_j\right] - \frac{\tilde{Q}_j}{\overline{h}} \partial_j U_i + \frac{H_i}{\rho \overline{h}} + \frac{\overline{\tau}_i^S - \overline{\tau}_i^B}{\rho \overline{h}} - \frac{1}{\overline{h}} \partial_t \tilde{Q}_j \tag{A2}$$

where the radiation S_{ij} and roller R_{ij} stresses are expressed as

$$S_{ij} = E^w \left(\frac{k_i k_j}{k^2} \frac{c^g}{c} + \delta_{ij} \left(\frac{c^g}{c} - \frac{1}{2}\right)\right) = \rho Q_i^w c_j^g + \rho \overline{h} J^w \delta_{ij} \tag{A3}$$

$$R_{ij} = c \left(\frac{\rho_r A_r}{T}\right) \left(\frac{k_i k_j}{k^2} + \frac{\delta_{ij}}{2}\right) = \rho Q_i^r c_j + \rho \overline{h} J^r \delta_{ij} \tag{A4}$$

respectively, in which J^w and J^r are defined as in equation (5). These decompositions are integrated into (A2) that becomes

$$\partial_t U_i + U_j \partial_j U_i + g\, \partial_i \overline{\zeta} = -\frac{1}{\overline{h}} \overbrace{\left[\partial_t \left(Q_i^w + Q_i^r\right) + \partial_j \left(Q_i^w \left(c_j^g + U_j\right) + Q_i^r \left(c_j + U_j\right)\right)\right]}^{\text{(WADBE)}} - \frac{Q_j^w + Q_j^r}{\overline{h}} \partial_j U_i - \frac{1}{\overline{h}} \partial_i \left[\overline{h} (J^w + J^r)\right] + \frac{H_i}{\rho \overline{h}} + \frac{\overline{\tau}_i^S - \overline{\tau}_i^B}{\rho \overline{h}} \tag{A5}$$

[40] Using the definitions of Q_i^w and Q_i^r, the term WADBE can be developed as follows:

$$\text{WADBE} = \frac{1}{\rho} \left[\frac{E^w + E^r}{\sigma_r} \partial_t k_i + \left(\frac{E^w}{\sigma_r} \left(c_j^g + U_j\right) + \frac{E^r}{\sigma_r} \left(c_j + U_j\right)\right) \partial_j k_i\right] + \frac{k_i}{\rho} \left[\partial_t \frac{E^w + E^r}{\sigma_r} + \partial_j \frac{E^w}{\sigma_r} \left(c_j^g + U_j\right) + \partial_j \frac{E^r}{\sigma_r} \left(c_j + U_j\right)\right] \tag{A6}$$

[41] The second part of (A6) highlights the wave action density equation due to both wave-organized motion and roller contribution (assuming that the relative frequency varies smoothly in time and space):

$$\partial_t \left(\frac{E^w + E^r}{\sigma_r}\right) + \partial_j \left[\frac{E^w}{\sigma_r} \left(c_j^g + U_j\right)\right] + \partial_j \left[\frac{E^r}{\sigma_r} \left(c_j + U_j\right)\right] = -\frac{D^r}{\sigma_r} \tag{A7}$$

Using the irrotationality of the wave number, the wave crest conservation equation [*Mei*, 1989] is written

$$\partial_t k_i + \left(c_j^g + U_j\right) \partial_j\, k_i = -k_j \partial_i U_j - \partial_{\overline{h}} \sigma_r\, \partial_i \overline{h} \tag{A8}$$

Thus, introducing (A7) in (A5), using the wave crest conservation equation (A8) and assuming that the wave velocity is equal to the group velocity (this approximation is verified in the surf zone), equation (A5) becomes

$$\partial_t U_i + U_j \partial_j U_i + g \partial_i \overline{\zeta} = \frac{k_i D^r}{\rho \overline{h} \sigma_r} + \frac{1}{\rho \overline{h}} \frac{E^w + E^r}{\sigma_r} \partial_{\overline{h}} \sigma_r\, \partial_i \overline{h} + \frac{\tilde{Q}_j}{\overline{h}} \left[\partial_i U_j - \partial_j U_i\right] - \frac{1}{\overline{h}} \partial_i \left[\overline{h} \tilde{J}\right] + \frac{H_i}{\rho \overline{h}} + \frac{\overline{\tau}_i^S - \overline{\tau}_i^B}{\rho \overline{h}} \tag{A9}$$

The dispersion relation enables the treatment of

$$\frac{E^w + E^r}{\sigma_r} \partial_{\overline{h}} \sigma_r = \frac{E^w + E^r}{\sigma_r} \frac{k}{\overline{h}} \left(\partial_k \sigma_r - \frac{\sigma_r}{2k}\right) = \frac{E_w + E_r}{c \overline{h}} \left(c^g - \frac{c}{2}\right) = \rho (J_w + J_r) \tag{A10}$$

[42] Finally, after a last simplification, the system of equations reads

$$\partial_t \overline{\zeta} + \partial_i \overline{h} U_i = -\partial_i \tilde{Q}_i \tag{A11}$$

$$\partial_t U_i + U_j \partial_j U_i + g \partial_i \overline{\zeta} = -\partial_i \tilde{J} + \frac{D^r k_i}{\sigma_r \rho \overline{h}} + \frac{\tilde{Q}_j}{\overline{h}} \left(\partial_i U_j - \partial_j U_i \right) + \frac{H_i}{\rho \overline{h}} + \frac{\overline{\tau}_i^S - \overline{\tau}_i^B}{\rho \overline{h}} \tag{A12}$$

[43] **Acknowledgments.** This Biscarrosse 2007 campaign was carried out thanks to the financial support of the BRGM. This study was performed within the framework of the ECORS (SHOM) project and the MODLIT (SHOM and INSU) project that have also sponsored this study. The authors thank the French Navy (SHOM) for the large bathymetry survey carried out on the studied field that was required for such an experiment. They are also grateful to the teams and students involved in the field experiment. The authors thank the developers of the models SWAN and MARS. The authors also thank André Fortunato for his comments and his help in improving the English quality of the paper. This work was partially funded by a postdoctoral research grant to the first author from the Fundação para a Ciência (SFRH/BPD/67041/2009). The third author acknowledges support from BARBEC (ANR 2010 JCJC 602 01). Finally, this work is dedicated to our friend and colleague Denis Michel, who tragically passed away during this field experiment.

References

Almar, R., B. Castelle, B. G. Ruessink, N. Sénéchal, P. Bonneton, and V. Marieu (2010), Two- and three-dimensional double-sandbar system behaviour under intense wave forcing and a meso–macro tidal range, *Cont. Shelf Res.*, *30*(7), 781–792, doi:10.1016/j.csr.2010.02.001.

Ardhuin, F. (2005), État de mer et dynamique de l'océan superficiel, Habilitation à diriger des recherches, thesis, Univ. de Bretagne Occidental, Brest, France.

Battjes, J. A. (1975), Modeling of turbulence in the surf zone, in *Proceedings of Symposium on Modelling Techniques*, vol. 2, pp. 1050–1061, Am. Soc. of Civ. Eng., San Francisco, Calif.

Battjes, J. A. (1988), Surf-zone dynamics, *Annu. Rev. Fluid Mech.*, *20*, 257–291, doi:10.1146/annurev.fl.20.010188.001353.

Battjes, J. A., and J. P. F. M. Janssen (1978), Energy loss and set-up due to breaking of random waves, in *Proceedings of Sixteenth Coastal Engineering Conference, Hamburg, Germany, Aug. 27–Sept. 3, 1978*, pp. 569–587, Am. Soc. of Civ. Eng., New York.

Bertin, X., A. B. Fortunato, and A. Oliveira (2009), A modeling-based analysis of processes driving wave-dominated inlets, *Cont. Shelf Res.*, *29*, 819–834, doi:10.1016/j.csr.2008.12.019.

Bonneton, P., N. Bruneau, B. Castelle, and F. Marche (2010), Large scale vorticity generation due to dissipating waves in the surf zone, *Discrete Contin. Dyn. Syst., Ser. B*, *13*(4), 729–738, doi:10.3934/dcdsb.2010.13.729.

Booij, N., R. C. Ris, and L. Holthuijsen (1999), A third-generation wave model for coastal regions 1. model description and validation, *J. Geophys. Res.*, *104*(C4), 7649–7666, doi:10.1029/98JC02622.

Brander, R. W. (1999), Field observations on the morphodynamic evolution of low wave energy rip current system, *Mar. Geol.*, *157*, 199–217, doi:10.1016/S0025-3227(98)00152-2.

Brander, R. W., and A. D. Short (2000), Morphodynamics of a large-scale rip current system at Muriwai Beach, New Zealand, *Mar. Geol.*, *165*, 27–39, doi:10.1016/S0025-3227(00)00004-9.

Brown, J., J. H. MacMahan, A. J. H. M. Reniers, and E. Thornton (2009), Surfzone diffusivity on a rip-channeled beach, *J. Geophys. Res.*, *114*, C11015, doi:10.1029/2008JC005158.

Bruneau, N. (2009), Modélisation morphodynamique des plages sableuses, Ph.D. thesis, Université Bordeaux I, Talence, France.

Bruneau, N., P. Bonneton, R. Pedreros, F. Dumas, and D. Idier (2007), A new morphodynamic modelling platform: Application to characteristic sandy systems of the Aquitanian Coast, France, *J. Coastal Res.*, *SI 50*, 932–936.

Bruneau, N., B. Castelle, P. Bonneton, R. Pedreros, J.-P. Parisot, and N. Sénéchal (2008), Modelling of high-energy rip current during Biscarrosse field experiment, in *31st International Conference on Coastal Engineering (ICCE 2008), Hamburg, Germany*, vol. 1, pp. 901–913, Am. Soc. of Civ. Eng., New York, doi:10.1142/9789814277426_0076.

Bruneau, N., B. Castelle, P. Bonneton, R. Pedreros, R. Almar, N. Bonneton, P. Bretel, J. Parisot, and N. Sénéchal (2009a), Field observations of an evolving rip current on a meso-macrotidal well-developed inner bar and rip morphology, *Cont. Shelf Res.*, *29*(14), 1650–1662, doi:10.1016/j.csr.2009.05.005.

Bruneau, N., B. Castelle, P. Bonneton, and R. Pedreros (2009b), Very low frequency motions of a rip current system: Drifter experiment and modeling, *J. Coastal Res.*, *SI 56*, 1731–1735.

Bühler, O. (2000), On the vorticity transport due to dissipating breaking waves in shallow-water flow, *J. Fluid Mech.*, *407*, 235–263, doi:10.1017/S0022112099007508.

Bühler, O., and T. E. Jacobson (2001), Wave-driven currents and vortex dynamics on barred beaches, *J. Fluid Mech.*, *449*, 313–339, doi:10.1017/S0022112001006322.

Butel, R., H. Dupuis, and P. Bonneton (2002), Spatial variability of wave conditions on the French Aquitanian Coast using in-situ data, *J. Coastal Res.*, *36*, 96–108.

Castelle, B., and P. Bonneton (2006), Modelling of a rip current induced by waves over a ridge and runnel system on the Aquitanian Coast, France, *C. R. Geosci.*, *338*, 711–717, doi:10.1016/j.crte.2006.06.003.

Castelle, B., P. Bonneton, N. Sénéchal, H. Dupuis, R. Butel, and D. Michel (2006), Dynamics of wave-induced currents over an alongshore non-uniform multiple-barred sandy beach on the Aquitanian Coast, France, *Cont. Shelf Res.*, *26*, 113–131, doi:10.1016/j.csr.2005.08.027.

Castelle, B., P. Bonneton, H. Dupuis, and N. Sénéchal (2007), Double bar beach dynamics on the high-energy meso-macrotidal french aquitanian coast: A review, *Mar. Geol.*, *245*, 141–159, doi:10.1016/j.margeo.2007.06.001.

Castelle, B., H. Michallet, V. Marieu, F. Leckler, J. Dubardier, A. Lambert, C. Berni, P. Bonneton, E. Barthélemy, and F. Bouchette (2010), Laboratory experiment on rip current circulations over a moveable bed: drifter measurements, *J. Geophys. Res.*, *115*, C12008, doi:10.1029/2010JC006343.

Dally, W. R. (2001), Modeling nearshore currents on reef-fronted beaches, paper presented at Fourth Conference on Coastal Dynamics, Am. Soc. of Civ. Eng., Lund, Sweden.

Dally, W. R., and C. A. Brown (1995), A modeling investigation of the breaking wave roller with application to cross-shore currents, *J. Geophys. Res.*, *100*(C12), 24,873–24,883, doi:10.1029/95JC02868.

Dingemans, M. W., A. C. Radder, and H. J. D. Vriend (1987), Computation of the driving forces of wave-induced currents, *Coastal Eng.*, *11*(5–6), 539–563, doi:10.1016/0378-3839(87)90026-3.

Haas, K. A., and J. C. Warner (2009), Comparing a quasi-3D to a full 3D nearshore circulation model: SHORECIRC and ROMS, *Ocean Modell.*, *26*, 91–103, doi:10.1016/j.ocemod.2008.09.003.

Haas, K. A., I. A. Svendsen, M. C. Haller, and Q. Zhao (2003), Quasi-three-dimensional modeling of rip current systems, *J. Geophys. Res.*, *108*(C7), 3217, doi:10.1029/2002JC001355.

Haller, M. C., and R. A. Dalrymple (2001), Rip currents instabilities, *J. Fluid Mech.*, *433*, 161–192.

Lazure, P., and F. Dumas (2008), An external-internal mode coupling for a 3D hydrodynamical model for applications at regional scale (Mars), *Adv. Water Resour.*, *31*(2), 233–250, doi:10.1016/j.advwatres.2007.06.010.

Longuet-Higgins, M. S., and R. W. Stewart (1964), Radiation stresses in water waves: A physical discussion, with applications, *Deep Sea Res.*, *11*, 529–563.

MacMahan, J. H., E. B. Thornton, T. P. Stanton, and A. J. H. M. Reniers (2005), Ripex—Rip currents on a shore-connected shoal beach, *Mar. Geol.*, *218*, 113–134, doi:10.1016/j.margeo.2005.03.019.

MacMahan, J. H., E. B. Thornton, and A. J. H. M. Reniers (2006), Rip current review, *Coastal Eng.*, *53*, 191–208, doi:10.1016/j.coastaleng.2005.10.009.

MacMahan, J. H., et al. (2010), Mean lagrangian flow behavior on an open coast rip-channeled beach: A new perspective, *Mar. Geol.*, *268*(1–4), 1–15, doi:10.1016/j.margeo.2009.09.011.

Madsen, O. S., Y.-K. Poon, and H. C. Graber (1988), Spectral wave attenuation by bottom friction: theory, paper presented at 21st International Conference on Coastal Engineering, Am. Soc. of Civ. Eng., Torremolinos, Spain.

Mei, C. C. (1989), *The Applied Dynamics of Ocean Surface Waves, Adv. Ser. Ocean Eng.*, vol. 1, World Sci., Singapore.

Özkan-Haller, H., and J. Kirby (1999), Nonlinear evolution of shear instabilities of the longshore current: A comparison of observations and computations, *J. Geophys. Res.*, *104*(C11), 25,953–25,984, doi:10.1029/1999JC900104.

Peregrine, D. H. (1998), Surf zone currents, *Theor. Comput. Fluid Dyn.*, *10*, 295–309, doi:10.1007/s001620050065.

Phillips, O. (1977), *The Dynamics of the Upper Ocean*, Cambridge Univ. Press, Cambridge. U. K.

Quartel, S. (2009), Temporal and spatial behaviour of rip channels in a multiple-barred coastal system, *Earth Surf. Processes Landforms*, *34*, 163–176, doi:10.1002/esp.1685.

Reniers, A. J. H. M., J. H. MacMahan, E. B. Thornton, and T. P. Stanton (2007), Modeling of very low frequency motions during ripex, *J. Geophys. Res.*, *112*, C07013, doi:10.1029/2005JC003122.

Reniers, A. J. H. M., J. H. MacMahan, E. B. Thornton, T. P. Stanton, M. Henriquez, J. W. Brown, J. A. Brown, and E. Gallagher (2009), Surf zone surface retention on a rip-channeled beach, *J. Geophys. Res.*, *114*, C10010, doi:10.1029/2008JC005153.

Reniers, A. J. H. M., J. H. MacMahan, F. J. Beron-Vera, and M. J. Olascoaga (2010), Rip-current pulses tied to Lagrangian coherent structures, *Geophys. Res. Lett.*, *37*, L05605, doi:10.1029/2009GL041443.

Smith, E., and N. Kraus (1990), Laboratory study on macro-features of wave breaking over bars and artificial reefs, *Tech. Rep. CERC-90-12*, U.S. Army Corps of Eng., Waterways Exp. Stn., Vicksburg, Va.

Smith, J. (2006), Wave-current interactions in finite depth, *J. Phys. Oceanogr.*, *36*(7), 1403–1419, doi:10.1175/JPO2911.1.

Stive, M. J. F., and H. J. De Vriend (1994), Shear stresses and mean flow in shoaling and breaking waves, paper presented at 24th International Conference on Coastal Engineering, Am. Soc. of Civ. Eng., (Kobe, Japan).

Svendsen, I. A. (1984), Wave heights and set-up in a surf zone, *Coastal Eng.*, *8*, 303–329, doi:10.1016/0378-3839(84)90028-0.

Thornton, E. B., J. H. MacMahan, and A. H. Sallenger Jr. (2007), Rips currents, mega-cusps, and eroding dunes, *Mar. Geol.*, *240*, 151–167, doi:10.1016/j.margeo.2007.02.018.

P. Bonneton and B. Castelle, Environnements et Paléoenvironnements Océaniques et Continentaux, UMR 5805, Université Bordeaux 1, CNRS, avenue des Facultés, F-33405 Talence, France.

N. Bruneau, Laboratório Nacional de Engenharia Civil, Av. do Brasil 101, P-1700-066 Lisboa, Portugal. (nbruneau@lnec.pt)

R. Pedreros, BRGM, 3 av. Claude-Guillemin, BP 36009, F-45060 Orléans CEDEX 2, France.